Nano- and Mesoscale Structure of $Na_{1/2}Bi_{1/2}TiO_3$: A TEM Perspective

Igor Levin and Ian M. Reaney*

The room-temperature structure of $Na_{1/2}Bi_{1/2}TiO_3$ (NBT) ceramics was studied using several transmission electron microscopy (TEM) techniques. High-angle annular dark field imaging in a scanning TEM confirmed an essentially random distribution of Bi and Na, while electron diffraction revealed significant disorder of the octahedral rotations and cation displacements. Diffraction-contrast dark-field and Fourier-filtered high-resolution TEM images were used to develop a model that reconciles local and average octahedral tilting in NBT. According to this model, NBT consists of nanoscale twin domains which exhibit $a^-a^-c^+$ tilting. The coherence length of the in-phase tilting, however, is limited to a few unit cells and is at least one order of magnitude shorter than that of anti-phase tilting. Assemblages of such nanodomains are proposed to exhibit an average $a^-a^-c^-$ tilt system. Diffuse sheets of intensity in electron diffraction patterns are attributed to local cation displacements correlated along both ⟨111⟩ and ⟨100⟩ chains and suggest partial polar ordering of these displacements. Overall, the TEM data indicate significant chemical, cation-displacement and tilt disorder of the NBT structure at the nano and mesoscale and support the premise that the *Cc* symmetry recently proposed from powder diffraction refinements is an averaged "best fit" cell.

1. Introduction

$Na_{1/2}Bi_{1/2}TiO_3$-based ceramics are among the most promising lead-free piezoelectric materials to compete with $Pb(Zr,Ti)O_3$ (PZT).[1–3] $Na_{1/2}Bi_{1/2}TiO_3$ (NBT) crystallizes with a perovskite-like structure and reportedly exhibits a sequence of phase transitions (on cooling) from high-temperature cubic (C,) to tetragonal (T) to room-temperature rhombohedral (R) structures[4]; the T and R phases appear to coexist over a rather broad (≈250 °C) temperature range. The transitions are associated with polar cation displacements and octahedral tilting.[4] According to Rietveld refinements using neutron powder diffraction data, the T phase (*P4bm*) exhibits in-phase $a^0a^0c^+$ [5] octahedral tilting and is weakly polar due to unequal antiparallel displacements of the A- and B-cations along the c-axis. The room-temperature rhombohedral structure has been refined as ferroelectric (*R3c*) with anti-phase tilting $a^-a^-a^-$ about the three cubic axes, although more recent studies of this phase[6,7] suggested a monoclinic (*Cc*) structure with $a^-a^-c^-$ tilting.

Detailed studies of NBT using transmission electron microscopy (TEM)[8–10] revealed that the local structure of this compound is very complex. In particular, superlattice reflections attributed to the in-phase and anti-phase tilting appeared to coexist in the entire temperature range and remained present as diffuse spots even in the high-temperature cubic phase. Electron diffraction patterns from the room-temperature R phase, which according to powder diffraction exhibited only anti-phase $a^-a^-a^-$ tilting, featured additional weak diffuse spots at locations corresponding to in-phase tilting. These diffuse spots were attributed to nanoscale precipitates of the T-phase ($a^0a^0c^+$ tilting) dispersed in a matrix of the R-phase ($a^-a^-a^-$).[8] The higher-temperature T-phase also featured coexistence of anti-phase and in-phase tilting diffraction reflections but their relative intensities were reversed with respect to room temperature.[10] Additionally, variable-temperature TEM studies revealed an intermediate orthorhombic structure with $a^-a^-c^+$ tilting.[9]

Despite intensive studies of NBT, many important aspects of its crystal structure remain elusive, which complicates analyses of NBT-based solid solutions. In fact, controversy exists over all aspects of the local atomic structure, including chemical Bi/Na ordering and the nature and coherence length of octahedral rotations and cation displacements. In the present study, various techniques of advanced transmission electron microscopy were applied to study NBT and develop a coherent structural model that reconciles the nano/mesoscale structural characteristics with the average structure refined using powder diffraction data.

2. Experimental Section

NBT samples for this study were prepared using conventional solid-state methods. Powders of Na_2CO_3 (A. R.), Bi_2O_3 (99.999%), and TiO_2 (<10 ppm phosphorus) were mixed by grinding using an agate mortar and pestle under acetone for 20 min, pressed into pellets, and calcined at 800 °C for 5 h. The calcined powders were ground using the same mortar and pestle for 15 min, pressed

Dr. I. Levin
Ceramics Division
National Institute of Standards and Technology
Gaithersburg MD 20899 USA
E-mail: igor.levin@nist.gov
Prof. I. M. Reaney
Department of Materials Science and Engineering
University of Sheffield
Sheffield, S13JD, UK

DOI: 10.1002/adfm.201200282

into pellets and sintered at various temperatures ranging from 800 °C to 1100 °C. The dwell times varied from 3 hours to 96 hours depending on temperature. The resulting samples were characterized using X-ray powder diffraction (XRD) and TEM. XRD measurements were performed using a Panalytical[1] X'Pert Pro X-ray powder diffractometer equipped with an incident beam monochromator (Cu $K\alpha_1$ radiation), Pixcel position sensitive detector, and an Anton Paar heating stage. A Philips CM-30 TEM (200 kV) and FEI Titan TEM/STEM (300 kV) equipped with a high-angle annular dark-field detector were used for TEM characterization. The TEM samples were prepared either by dispersing NBT powders on lacey-carbon coated support grids or by mechanical polishing followed by dimpling and ion-thinning until perforation. Selected samples were annealed at 600 °C for 2 h after dimpling and prior to ion-thinning to remove remaining residual stresses.

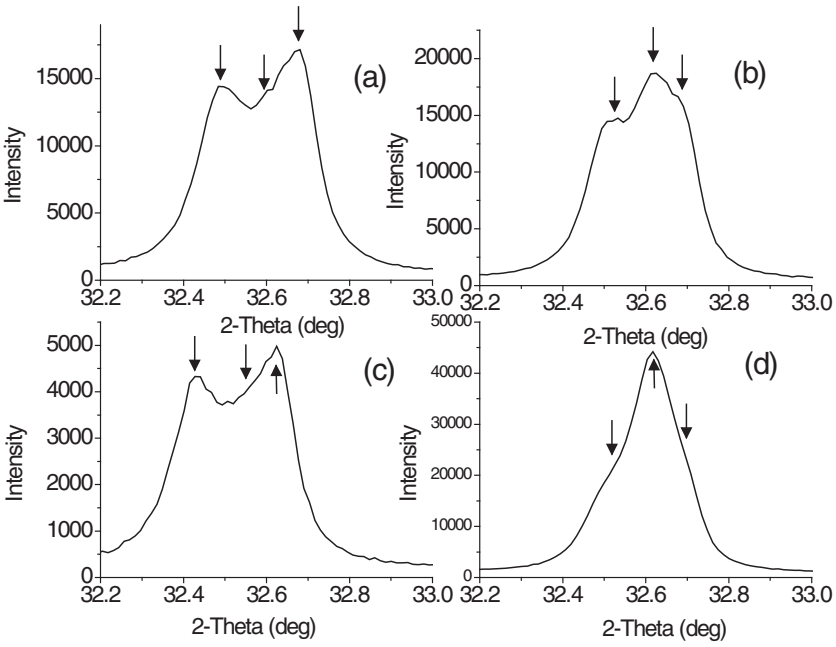

Figure 1. X-ray diffraction 110 perovskite reflection measured for NBT sintered at (a) 950 °C for 96 h, (b) 1000 °C for 5 h, and (c) 1100 °C for 3 h. The data were collected on powders obtained by grinding the sintered pellets. Trace (d) was measured on the powder that was first sintered at 950 °C (i.e. (a)), ground, and then additionally annealed at 600 °C. Annealing the ground powder in the cubic-phase field causes marked irreversible changes in the appearance of the 110 reflection. None of the traces can be described using a rhombohedral structure, which would feature a doublet, whereas all measured profiles reveal the presence of at least three overlapping peaks. Reheating the ground powders that were sintered at 1000 °C and 1100 °C produced similar results.

3. Results and Discussion

3.1. The Effect of Thermal and Mechanical History on NBT Structure

As reported previously,[6,7] calcination of NBT at 800 °C yielded a single perovskite phase with relatively broad diffraction peaks that were indexed according to a cubic cell with a = 3.88(1) Å. TEM analyses of calcined powders revealed strong sharp superlattice reflections due to anti-phase octahedral tilting along with the associated twin domains; overall, these patterns and images were consistent with an *R3c* phase, which features an $a^-a^-a^-$ tilt system. Post-calcination heat-treatment (e.g. 950 °C) resulted in splitting of the cubic *hk0* reflections, as expected for a rhombohedral structure. However, these reflections split into at least three peaks (**Figure 1**), which cannot be accounted for by rhombohedral distortion. Annealing ground powders at 600 °C for 2 h modified the splitting and yielded diffraction patterns and 110 reflection profiles (Figure 1, trace (d)) similar to those reported for a monoclinic *Cc* structure refined using synchrotron-radiation X-ray diffraction data.[7]

Our results suggest a strong effect of thermal and mechanical history on the average structural distortion in NBT. In particular, residual stresses, induced in this instance via grinding, significantly modify the average structural distortion. The exact mechanism of this effect, which could be exploited to tailor the NBT properties, has yet to be determined, but one plausible reason includes ferroelastic poling. Interestingly, such extreme sensitivity to residual stress in piezoelectrics is commonly associated with compositions close to a morphotropic phase boundary, where phase assemblages may be altered and peak splitting enhanced by surface grinding.

3.2. Electron Diffuse Scattering

Room-temperature selected-area electron diffraction patterns of NBT are summarized in **Figure 2**. These patterns exhibit sharp and strong ½{*ooo*} spots (hereafter, "*o*" and "*e*" refer to odd and even *hkl* indexes, respectively) that are consistent with rhombohedral *R3c* or *Cc* structures.[4] However, the ⟨103⟩ patterns reveal linear ⟨100⟩ rods of diffuse intensity (confirmed by sample tilting), which pass through ½{*ooo*} reflections and imply local deviations from rhombohedral symmetry. These diffuse rods have been reported in previous studies of NBT[8] and were attributed to disordered (in-phase/anti-phase) rotations of oxygen octahedra. Significant condensation of diffuse intensity at ½{*ooe*} locations is best explained by the presence of short-range-ordered in-phase octahedral rotations[2].

1) Certain commercial equipment is identified in order to specify adequately the experimental procedure; recommendation or endorsement by the National Institute of Standards and Technology is not therein implied.

2) Alternatively, these diffuse spots could be attributed to short-range-ordered anti-parallel cation displacements as occur in PZT [11] and $BiScO_3$-$PbTiO_3$ [12]. However, such cation displacements are expected to generate ½*hk0* (h = k) reflections, which remain notably extinct in NBT (Figure 2).

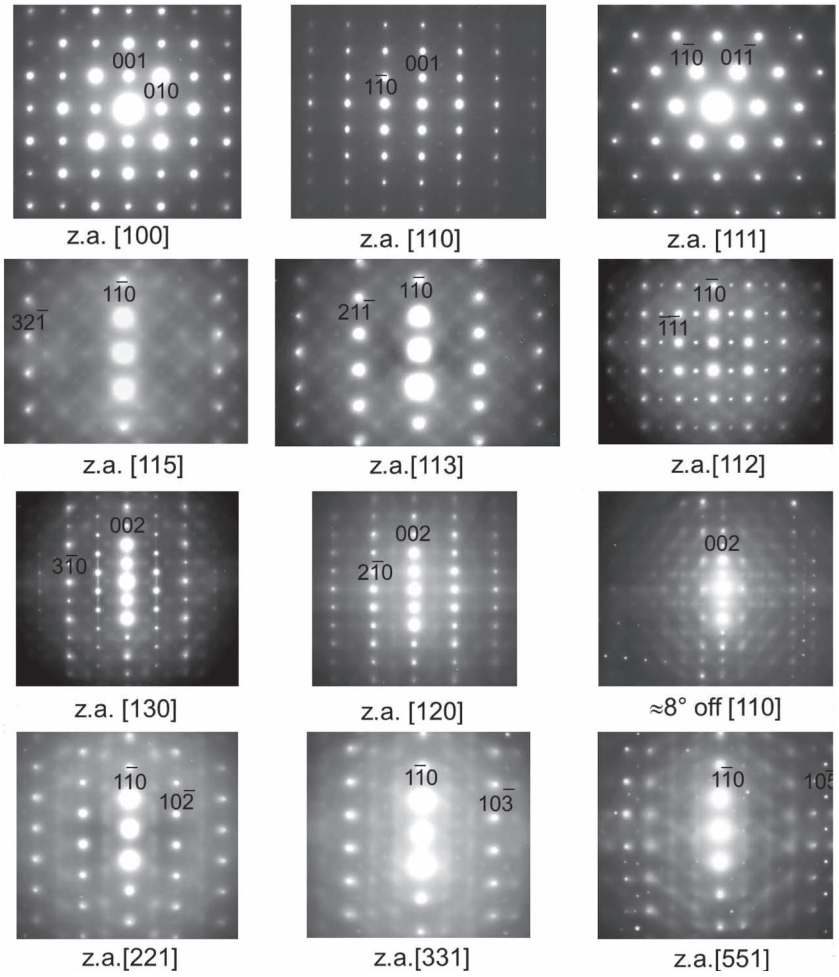

Figure 2. A series of electron diffraction patterns recorded from the single grain of NBT. The fundamental reflections are indexed according to a cubic perovskite cell. The [130] and [112] patterns exhibit sharp superlattice reflections at ½{*ooo*}. A complex structured diffuse scattering is revealed. This scattering consists of ⟨100⟩ rods of diffuse intensity passing through ½{*ooo*} reflections (seen in [130] orientation) and diffuse {100} and {111} sheets. Traces of the {100} sheets appear prominently in [115], [113], and [112] orientations, whereas traces of the {111} sheets are clearly visible in the [221], [331] and [551] patterns. The [120] and [130] patterns feature detectable traces of both the {100} and {111} sheets. The round-shaped diffuse spots seen in all of the patterns correspond to enhanced intensity at the intersections of the diffuse sheets.

In addition to these linear rods of intensity, high-index zone-axis diffraction patterns of NBT exhibit diffuse-scattering streaks consistent with traces of {111} and {100} planes. The {111} traces are extinct through the origin and pass only through reflections with $h+k+l = 2n$. The visibility of the {100} and {111} traces *differs* for different zone axes. The {100} traces are seen clearly in ⟨11*l*⟩-type sections whereas the {111} traces appear prominently in ⟨10*l*⟩ and ⟨*hhl*⟩ orientations (all the patterns were recorded from the same area). The reasons for such different visibility of {100} and {111} diffuse sheets are unclear; possible explanations include non-uniform distribution of intensity along the sheets and different angles between these sheets and the reciprocal-lattice sections.

The {111} diffuse sheets in NBT are similar to those observed in PZT[13,14] and NBT-based solid solutions.[15] By analogy with PZT, these sheets can be attributed to linear correlations among the A- and B-cation ⟨111⟩ displacement components along ⟨111⟩ directions. In the model proposed by Baba-Kishi *et al.*[13], both A- and B-cations are displaced along ⟨111⟩ (to account for extinctions of diffuse scattering through reflections $h+k+l = 2n+1$) and their displacements are correlated along the -A-B-A- chains. The transverse correlations among such chains were assumed to be zero. Random displacements along all ⟨111⟩ directions yield an 8-site probability distribution for the cations in the cubic phase.[13,14] In the framework of the order-disorder model, phase transitions from the cubic to tetragonal and rhombohedral phases are accompanied by appropriate changes in the relative probabilities of the cations populating these 8 sites. For example, a model that accounts for the presence of all the {111} diffuse sheets in the rhombohedral structure involves preferential (i.e., probability larger than 1/8) cation displacements along one of the ⟨111⟩ directions, with the remaining probability (<7/8) being equally partitioned between the other ⟨111⟩ directions.[14]

The origin of hitherto unreported {100} diffuse sheets in NBT is less obvious. Their appearance differs from that of the {100} diffuse sheets in $BaTiO_3$[16], $KNbO_3$[16], and $AgNbO_3$[17], where the diffuse scattering arises due to linear-chain correlations of the B-cation and oxygen displacements. In principle, the {100} diffuse sheets in NBT can be associated with octahedral tilting disorder, which is expected to generate both rods of diffuse intensity through ½{*ooo*} *and* ½{*ooe*} spots (seen in ⟨103⟩ patterns) and {100} diffuse sheets through the fundamental reflections.[18] For typical values of the scattering vector, the intensity in these diffuse sheets should be at least a factor of 20 lower than that in the diffuse rods[18], but a reliable estimate of such intensity ratios from experimental electron diffraction patterns is difficult. Alternatively, the {100} diffuse sheets may reflect cation displacements correlated along ⟨100⟩ directions. Unlike the {111} diffuse scattering, the {100} sheets exhibit no obvious extinction through the origin. This lack of the so-called "transverse polarization"[19] would be expected if {100} sheets originated from tilting. Alternative explanations one would require either chemical ordering or correlations of atomic displacement components that are inclined to the ⟨100⟩ correlation directions. Short-range chemical ordering on the A-sites that maintains stoichiometry and, therefore, charge neutrality for the perovskite unit cell (i.e. a mixture of six clusters in Figure 2 of Ref. 20) would generate three sets of diffuse {100} sheets but passing through $\mathbf{g} = ½\ \langle h00\rangle^*$ ($h = 2n+1$)[21]; that is, *between* the Bragg reflections. Thus, common types of chemical ordering cannot contribute to the presently observed {100} sheets, which pass *through* the Bragg reflections.

In all of the reciprocal lattice sections, the diffuse scattering is significantly enhanced at the intersections of traces corresponding to the different sets of {100}/{111} sheets; the enhancement appears to be stronger than expected for a simple superposition of the traces. Thus, the overall diffuse intensity distribution can be better described as a superposition of the {100} and {111} diffuse sheets and diffuse rods that coincide with the intersections of these sheets. The enhanced diffuse intensity (beyond normally expected) along the line [*uvw*] of intersection for the two (or more) diffuse intensity sheets suggests that the real-space linear chains, which generate these diffuse sheets, become correlated in the planes normal to [*uvw*] thus giving rise to the [*uvw*] diffuse rods. Such diffuse scattering distribution is inconsistent with octahedral tilting disorder. Thus, the {100} sheets are more likely related to correlated cation displacements. Diffuse scattering calculated for a simplified model that incorporates A- and B-cation displacements correlated simultaneously along the ⟨111⟩ and ⟨100⟩ chains reproduces the diffuse spots observed in the experimental diffraction patterns, even though these simulations still cannot explain the different visibilities of the {111} and {100} traces in different orientations. Detailed studies of 3-D diffuse intensity distribution using the rotation method[22] could help to resolve this issue.

In summary, electron diffuse scattering indicates a coexistence of octahedral tilting disorder (diffuse rods) and disordered displacements of the A- and B-cations (diffuse sheets). The cation displacive disorder can be attributed to local cation shifts along the ≈⟨111⟩ directions. Plausibly, a sequence of C↔T↔R(M) phase transitions in NBT is accompanied by changes in the type of partial ordering of ⟨111⟩ displacements from the 8-site cation distribution in the cubic structure to a 4-site distribution (4 equal-probability sites forming a face of a cube) in the tetragonal phase to a (1 + 7)-site distribution in the rhombohedral phase. In the rhombohedral structure, 1 of the 8 sites is occupied preferentially, whereas the probability distribution over the remaining 7 sites has to obey rhombohedral symmetry; the latter requirement is lifted if the actual symmetry of the low-temperature phase is monoclinic. The correlations among the cation displacements likely involve not just ⟨111⟩ but also ⟨100⟩ chains, as manifested in the {100} diffuse sheets. Previous XAFS studies[23] indicate that the magnitude of local Ti off-centering in NBT remains approximately constant across the phase transitions from the room-temperature rhombohedral/monoclinic to the high-temperature cubic structure. This result is consistent with the order-disorder character of the phase transitions (as far as the cation displacements are concerned) suggested by the diffuse scattering. Ti EXAFS data could not be fitted assuming either ⟨111⟩ or ⟨100⟩ Ti displacements[24], which appears to be at odds with the ⟨111⟩ displacements inferred from the polarized appearance of {111} diffuse-scattering sheets; however, as EXAFS probes pair correlations, the discrepancy could be caused by disordered oxygen displacements that contribute to local distortions of [TiO_6] polyhedra.

3.3. Distribution of Bi and Na

Chemical ordering of Bi and Na remains debatable. First principles calculations[20,24] suggested several candidate ordered structures but none of these have been experimentally verified. Yet, a number of experimental studies speculated on the existence of chemical Bi/Na ordering. For example, Dorcet *et al*[9], proposed rocksalt-type ordering to explain residual intensities of ½{*ooo*} reflections at high temperature, even though this type of ordering has been discarded by theoretical calculations at least at 0 K. The absence of sharp superlattice reflections due to Bi/Na ordering in X-ray diffraction patterns indicates that any ordered arrangements, if present, are limited to the nanoscale. Thus, models that assumed ordered nanodomains in the disordered matrix have been suggested.[19] Ordered superstructures in the form of nanodomains are expected to generate diffuse superlattice reflections. The experimental evidence available to date rules out several superstructures that have been proposed as the most stable for NBT from first-principles calculations. For example, both the {001} layered model[20] (*P4/mmm*, $c = 2a = 2a_0$, where a_0 is the lattice parameter of an ideal cubic perovskite) and a "criss-cross" model[23] ($P4_2/mmc$, $a = b = c = 2a_o$) generate ½{*eeo*} diffraction spots; however, no such reflections could be detected in the experimental electron diffraction patterns or FFT patterns obtained from the appropriate HRTEM images. In the case of rocksalt-type ordering, which generates eight equivalent ½{*ooo*} spots, the situation is more subtle because these spots could be masked by the sharp superlattice reflections associated with anti-phase tilting. The ½{*ooo*} diffraction spots due to tilting are extinct in the ⟨110⟩ orientation parallel to ⟨11.0⟩ directions of the rhombohedral structure (or [010] direction in the monoclinic *Cc*); however, a fine scale of rhombohedral/monoclinic twin domains (see the next section) precludes the use of selected area electron diffraction. Previous high-resolution TEM studies of NBT, which focused on the search for reportedly stable Bi/Na arrangements[25], were limited to ⟨100⟩ orientations that are insensitive to rocksalt-type ordering.

In the present work, we used high-resolution high-angle annular dark field (HAADF) imaging in STEM to probe cation distributions in the sample. This imaging mode is often referred to as "Z-contrast" to emphasize its sensitivity to atomic numbers. Therefore, a spatial distribution of Bi (Z = 83) and Na (Z = 11) is expected to appear prominently in HAADF images. As NBT is prone to radiation damage, a series of images were acquired using short recording times (10 s per frame) and then averaged (after correcting for drift) to improve counting statistics. The data were collected on NBT particles dispersed on a lacey carbon film on a support grid to avoid any potential ion-milling artifacts. The samples were subjected to very gentle plasma cleaning (using a special shielded sample holder designed for slow etching of carbon) prior to inserting it into TEM to avoid build-up of contamination.

The HAADF images recorded in both ⟨100⟩ and ⟨110⟩ orientations (from separate crystals) reveal no well-defined nanoscale order (**Figure 3**). The FFT transforms from the {100} images exhibited no hint of superlattice spots. The FFT from some {110} images exhibit sharp ½{*ooo*} spots associated with anti-phase tilting whereas the FFT from others (shown here) contain only fundamental reflections, which is consistent with reflection conditions for *R3c* or *Cc* structures. The mesoscale variations of contrast in the [110] image are likely related to thickness-variation effects. Some contrast variations among the adjacent columns suggest a heterogeneous distribution of

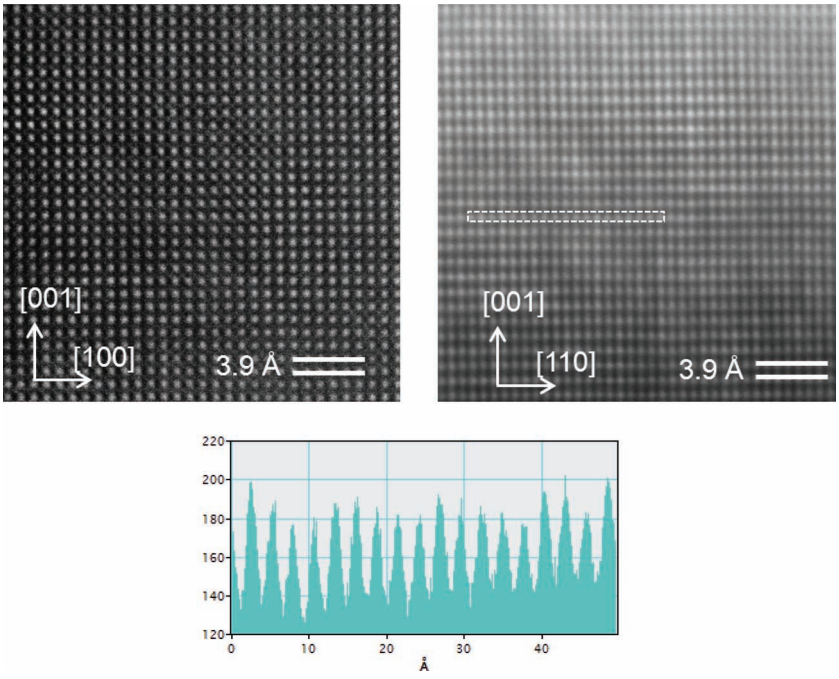

Figure 3. (Top) High-angle annular dark-field STEM images recorded from NBT in ⟨100⟩ (left) and ⟨110⟩ (right) zone axis orientations. Bright spots in both images correspond to the A-site (Bi/Na) columns. These images reveal no obvious nanoscale Bi/Na order. Some image distortion is an artifact of the drift during image acquisition. (Bottom) A representative intensity profile for the A-site columns along the [110] direction obtained from the [110] image (the profile corresponds to a band indicated in the image). The profile features column-to-column intensity variations suggesting a somewhat heterogeneous distribution of Bi and Na but displays not obvious ordering pattern.

Bi and Na (Figure3, bottom); however, no well-defined ordered pattern is observed. These results do not support the proposed models of ordered NBT nanodomains. Note that nanodomains with B-site ordering have been readily detected in HAADF STEM images of $PbMg_{1/3}Nb_{2/3}O_3$ despite much weaker contrast and domain overlap along the beam direction.[26] As discussed in the previous section, the absence of diffuse {100} sheets at $\mathbf{g} = ½\langle h00\rangle^*$ (h odd), rules out any significant short-range order in the form of A-site cubic clusters having a 1:1 ratio of Bi and Na.

3.4. Domain Structure

Figure 4 shows two dark field images of the same single grain in NBT (x = 0) which reveal the domain structure associated with $\mathbf{g}_1 = ½[\bar{1}31]^*$ and $\mathbf{g}_2 = ½[1\bar{1}3]^*$ reflections in the [310] and [013] zone axes, respectively. The curved ribbon-like defects correspond to anti-phase boundaries attributed to the impingement of two regions of tilt which have nucleated out of phase. These relatively large-scale (hundreds of nm) anti-phase domains (APD) contain a much finer-scale (10 nm to 50 nm) twin-domain substructure. The contrast variance among the twin variants is associated with distinct intensities of the ½311 and ½ 31$\bar{1}$-type reflections; images of the same area using these reflections (not shown) exhibited a complementary contrast. In a given grain, the twin boundaries reside preferentially on one set of {100} planes (i.e. (001) in Figure 4) and therefore appear edge-on in the [310] zone-axis pattern but inclined to the beam in [031] orientation. Note the absence of twin-domain boundaries on the (100) planes in Figure 3b. This preferential alignment of twin-domain boundaries is consistent with the shape of ½{*ooo*} spots which appear elongated along the [001] direction in Figure 4a but round in the second orientation in Figure 4b. The relative fractions of inequivalent twin domains varied from grain to grain; however, the majority of grains featured extended areas with twin interfaces residing on a single set of {100} planes. Qualitatively similar results were obtained on several independently prepared TEM samples, including those that were annealed in the cubic-phase field after mechanical polishing and prior to ion thinning to remove residual stresses.

The high number density of {100} twin-domain boundaries suggests their low energy. The {100} domain walls are invariant in the rhombohedral structure and provide effective accommodation of the transformation strain.[27] Octahedral tilting can remain continuous across these {100} boundaries with little distortion of octahedra if (i) the twinning operation corresponds to a planar fault in the tilting sequence (i.e. $a^-a^-c^+$ instead of $a^-a^-a^-/a^-a^-c^-$) around the cubic axis oriented normal to the boundary and (ii) the boundary itself passes through the octahedra vertices rather than the B-sites.[28] In the structure, which exhibits octahedral tilting around a single cubic axis (e.g. the tetragonal high-temperature phase), such tilting

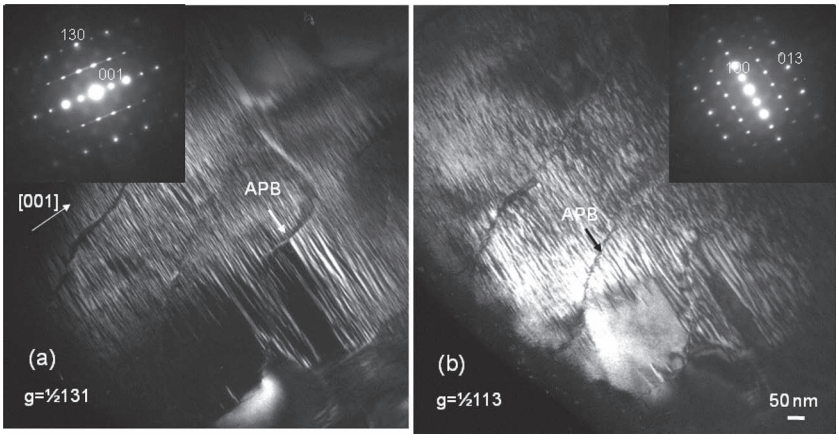

Figure 4. Dark-field images and corresponding $\langle 103\rangle_p$ electron diffraction patterns recorded from a single grain of NBT. The angle between the two $\langle 103\rangle_p$ orientations is ≈25°. The images and diffraction patterns are shown as recorded without correcting for image rotation.

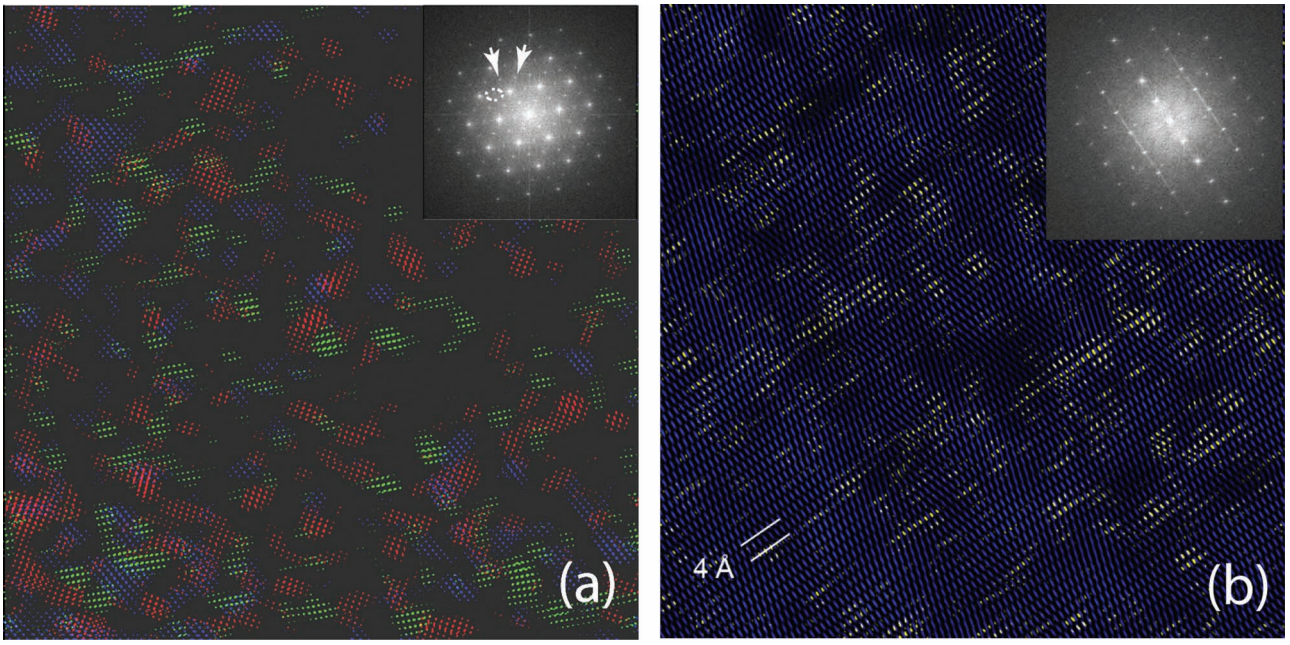

Figure 5. a) RGB HRTEM image of NBT in [111] orientation reconstructed from the three images obtained by filtering the raw image using three distinct sets of ½{*ooe*} spots, clearly visible in the image FFT (inset). Each color (i.e. red, green, and blue) represents a single variant of these spots. The image suggests a relatively uniform mixture of the variants on the scale smaller than the scale of the twin variants (15-20 nm). Note unequal fractions of the three variants as manifested prominently in the weaker intensity of one set of the ½{*ooe*} spots (circled using dotted line) in the FFT. b) A colored version of the Fourier-filtered HRTEM image of NBT in the [130] orientation. This image is a superposition of the two images: yellow, filtered using the diffuse intensity centered on ½{*ooe*} and, blue, filtered using the superlattice spots at ½{*ooo*}. An image reconstructed using the ½{*ooo*} reflections only (not shown) exhibits undisturbed fringes.

faults would yield anti-phase boundaries, not twins. However, in the system with octahedral tilting around all three cubic axes, an anti-phase boundary results from coincident faults in the tilting sequences about all three axes, whereas a single fault is equivalent to a twinning operation. In the presence of average octahedral tilting $a^-a^-a^-$ and a strong tendency toward tilting disorder, an intuitive energetic perspective suggests that most tilting faults would be coincident with ferroelastic/ferroelectric twin boundaries. The net polarization vectors in these twin domains are expected to be directed along the appropriate non-equivalent ≈⟨111⟩ directions. Fine scale of pseudo-rhombohedral twin domains, which reside preferentially on particular {100} planes, resembles adaptive structures that were encountered near morphotropic phase boundaries in $Pb(Mg_{1/3}Nb_{2/3})O_3$-$PbTiO_3$ and several other related systems.[29] Moreover, the coincidence of ferroelastic/ferroelectric twin walls with APB's has been illustrated in low temperature studies of the R-phase in PZT by Randall and co-workers.[30]

Visible condensation of diffuse intensity at ½{*ooe*} locations indicates locally-ordered in-phase tilting. Fourier transforms of the high-resolution TEM images recorded in ⟨103⟩ zone-axis orientations (**Figure 5**) exhibit both ½{*ooe*} diffuse spots and ⟨100⟩ diffuse streaks suggesting that the information on these correlations is encoded in the images. Fourier filtering using the ½{*ooe*} diffuse spots highlights regions that are a few unit cells thick along the ⟨100⟩ direction and are elongated in the (100) planes. Similar Fourier-filtered imaging using ½{*eoo*}, ½{*ooe*}, and ½{*oeo*} diffuse spots in ⟨111⟩ orientation confirms a superposition of the three variants associated with each of these reflections, which occupy spatially-distinct regions. In Figure 5a, these variants are represented using different colors (red, green, and blue). Thus, imaging the ½{*ooe*} -type reflections in the two orientations indicates that each variant features in-phase tilting along one of the three cubic axes. The fractions of the three variants appear to be unequal over the area sampled by this image, as evident in the weaker intensity of one set of ½{*ooe*} spots in the corresponding FFT. Clearly, the thicknesses of the in-phase tilted regions (1 nm to 3 nm) are an order of magnitude smaller than the thicknesses of the pseudo-rhombohedral twin domains (10 nm to 40 nm) identified in the dark-field images in Figure 4. The actual aspect ratio (lateral scale/thickness) of the in-phase tilted regions is difficult to assess from the FFT-filtered images because it depends on the extent of the diffuse streak included in the inverse Fourier transform.

Thus, the domain structure of NBT is extremely complex and spans several scale lengths. The T↔R/M phase transition associated with the onset of the net polar displacements and average anti-phase tilting (i.e. $a^-a^-a^-$or $a^-a^-c^-$) gives rise to mesoscale anti-phase domains and nanoscale twin domains; the latter represent regions where octahedra rotate around non-equivalent ≈⟨111⟩ directions. The tilting twin domains apparently coincide with non-180° ferroelectric domains associated with distinct directions of the net polarization. These twin domains contain three variants of even finer-scale twin domains, which feature one in-phase tilting component. A given ⟨100⟩ octahedral chain in NBT exhibits a non-periodic sequence of longer sections featuring *anti-phase* tilting mixed with shorter sections of *in-phase* tilting. The transverse correlations of rotations in

the neighboring chains extend over relatively large distances so that the regions having the *in-phase* tilting component acquire platelet-like shapes. This mixed tilting occurs along all three cubic axes.

3.5. A Model of Octahedral Tilting Disorder

The exact interpretation of the tilting disorder is debatable. *Dorcet et. al.*[8] assumed discreet tetragonal-like precipitates with $a^0a^0c^+$ tilting dispersed in a $a^-a^-a^-$-tilted rhombohedral matrix. In the following discussion, we argue that the available HRTEM and electron diffraction data are much better interpreted in terms of pseudo-rhombohedral assemblages of nanoscale orthorhombic domains that exhibit $a^-a^-c^+$ tilting. The coherence length of in-phase tilt which defines the dimensions of the nanodomains is at least an order of magnitude less than that of anti-phase tilting. We therefore conclude that NBT is best described by a *single-phase* "continuous tilting" model in which each orthogonal axis exhibits short-range ordered in-phase tilting superimposed on long-range ordered anti-phase tilting. The distribution and size of the $a^-a^-c^+$ nanodomains presumably relates to the Na/Bi distribution. This single-phase model is thus markedly different from the two-phase model suggested by Dorcet et al.[8,9]

HRTEM images simulations in the ⟨130⟩ orientation using the MacTempas/CrystaKit software package suggest that tetragonal ($a^0a^0c^+$) regions should produce a rather distinct contrast compared to that of the anti-phase-tilted ($a^-a^-a^-$ or $a^-a^-c^-$) matrix, even if these precipitates overlap with the matrix in the direction of an electron beam. In particular, simulations predict that lattice fringes associated with ½{*ooo*} reflections should exhibit visible disruptions/distortions across the tetragonal regions with exclusive in-phase tilts. However, no such distortions could be observed in the Fourier-filtered experimental images, which, therefore disfavor the "tetragonal precipitate" model. The HRTEM contrast for the $a^-a^-c^+$ and $a^-a^-a^-$ (or $a^-a^-c^-$) structures is far more similar and the g = ½{*ooo*} fringes remain relatively undistorted across the interfaces; that is, our HRTEM results are consistent with the $a^-a^-c^+$ model. The $a^-a^-c^+$ tilting, which in the absence of polar order generates orthorhombic *Pnma* symmetry, is typically accompanied by anti-parallel A-cation displacements along the ⟨110⟩ direction aligned with the orthorhombic *a*-axis that give rise to ½{*eeo*} reflections; otherwise, these reflections would remain very weak and practically undetectable. Electron diffraction patterns of NBT reveal no hint of ½{*eeo*} reflections–a result that has been used as an argument against domains with $a^-a^-c^+$ tilting.[8] However, the structured diffuse scattering indicates disordered cation displacements along ⟨111⟩ directions which could cause disorder of the ⟨110⟩ displacement components that dominate the intensities of the ½{*eeo*} reflections. The ferroelectric nature of the *R*/*M* phase implies net average polar displacements, but purely ferroelectric displacements provide no significant contribution to the ½{*eeo*} reflections which, therefore, could remain undetectable. Ferroelectric $BiInO_3$[31] is an example of a structure that combines $a^-a^-c^+$ octahedral tilting with polar cation displacements along ⟨111⟩ directions, which yield $Pn2_1a$ symmetry (a subgroup of *Pnma*); however, unlike NBT, in $BiInO_3$, the ⟨110⟩ components of cation displacements are ordered in the antiparallel pattern.

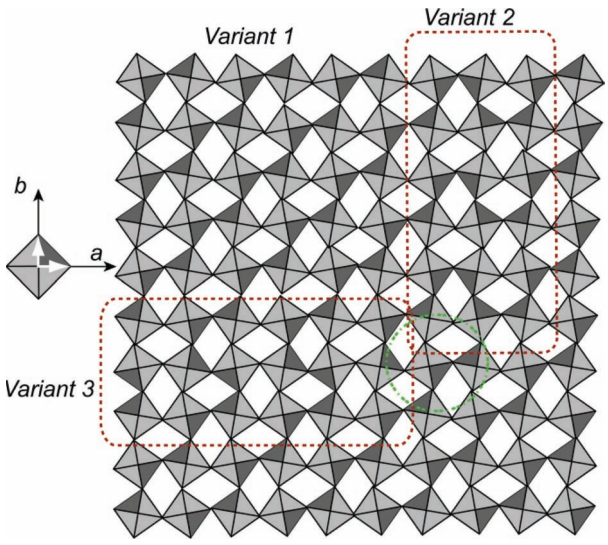

Figure 6. A schematic 2-D rendering of an assemblage of three variants exhibiting $a^-a^-c^+$ tilting as viewed along the cubic perovskite axis. The octahedra are represented using squares. The directions of rotations around the in-plane "*a*" and "*b*" axes (white arrows on the left) are indicated using a color code: the combined vector of rotation for a given octahedron points toward the dark grey quadrant. The coherence length of the in-phase tilting is significantly shorter than that of the anti-phase tilting (the actual *relative* thickness of domains along the in-phase tilting direction is appreciably shorter than shown in the schematics). Variant 1 exhibits in-phase tilting along the viewing direction. Anti-phase tilting dominates for all the octahedral chains.

An assemblage of three coherent platelet-like orthorhombic $a^-a^-c^+$ variants having long- (>5 nm to 10 nm) and short (1-2 nm) coherence lengths for the anti-phase and in-phase rotations, respectively, results in the *average anti-phase* tilting along any octahedral chain, thus yielding a pseudo-rhombohedral or monoclinic structure when averaged over a scale of > ≈10 nm (**Figure 6**). The relative magnitude and the directions of octahedral rotations about the three cubic axes can vary continuously to accommodate the strain associated with boundaries between the differently oriented $a^-a^-c^+$-tilted regions. A single nanodomain of NBT can be seen as having a continuously varying tilt order-parameter along one axis whereas the two remaining orthogonal axes have fixed amplitudes of anti-phase rotations. Despite the disorder, each pseudo-rhombohedral twin domain exhibits its specific predominant ≈⟨111⟩ tilting axis.

Thus, we propose that the NBT structure at room temperature exhibits a coherent assemblage of the three nanoscale domain variants featuring local $a^-a^-c^+$ tilting which averages to $a^-a^-a^-/a^-a^-c^-$ tilting over the scale probed by X-ray diffraction due to a very short coherence length of the in-phase tilting component. Our model assumes that chemical A-site disorder combined with this short coherence length of the in-phase rotations are insufficient to promote ordering of the anti-parallel A-cation displacements, and the cation displacements remain somewhat decoupled from tilting. The net polarization direction on the nanoscale scale is likely to deviate from the average polarization direction, but these deviations cannot be ascertained from the TEM data. Unequal fractions

of the pseudo-orthorhombic variants (see the FFT pattern and the caption in Figure 5a) sampled by X-ray diffracting volumes could contribute to the apparent distortions from the average rhombohedral structure identified using X-ray diffraction.

The "continuous tilting" model reflects a competing nature of the anti-phase and in-phase tilting in NBT. At a given temperature the dominant tilting mode exhibits significantly larger coherence length than the non-dominant one, and this larger coherence length determines the average structural distortion seen by X-ray diffraction. According to our model, the intermediate-temperature orthorhombic *Pnma* structure, detected by Dorcet et al[9], evolves from the room-temperature state by increasing the coherence length of the in-phase tilting, which becomes more favored at higher temperatures, and this larger coherence length stabilizes ordering of the anti-parallel A-cation displacements. This mechanism differs from the periodic arrangement of the twin domain boundaries within the rhombohedral phase as proposed in Ref. [9].

4. Conclusions

TEM studies of NBT indicate a co-existence of chemical (Bi/Na) and displacive (octahedral tiling and cation displacements) disorder. At room-temperature, NBT is proposed to consist of nanoscale domains that feature $a^-a^-c^+$ tilting, where the coherence length for in-phase tilting extends over just a few perovskite unit cells, and is much shorter than the coherence length for anti-phase tilting about two other cubic axes. Thus, the domain averaging yields an anti-phase tilted, $a^-a^-a^-(c^-)$ pseudo-rhombohedral structure. The short coherence length of the in-phase tilting accounts for the ⟨100⟩ rods of diffuse intensity. Our HRTEM results indicate inequivalent fractions of the three nanoscale $a^-a^-c^+$-tilted domains over a sub-20 nm length-scale, which can explain an average monoclinic distortion due to $a^-a^-c^-$ (rather than $a^-a^-a^-$) tilting as seen by X-ray diffraction. Cation displacements exhibit substantial disorder, with ≈⟨111⟩ displacements that appear to be correlated along both ⟨111⟩ and ⟨100⟩ chains thus giving rise to {111} and {100} sheets of diffuse intensity; a partial polar ordering of the cation displacements is indicated by previous structural refinements and dielectric measurements. Such a highly complex local structure of NBT presents challenges for powder diffraction techniques as any meaningful local-structure model would have to account for the spatially-resolved TEM observations.

Acknowledgements

Useful discussions with Victor Krayzman (NIST) and his help with simulations of diffuse scattering are acknowledged.

Received: January 30, 2012
Revised: March 15, 2012
Published online: May 18, 2012

[1] T. Takenaka, K. Maruyama, K. Sakata, *Jpn. J. Appl. Phys. Part 1 - Regul. Pap. Short Notes Rev. Pap.* **1991**, *30*, 2236.
[2] T. R. Shrout, S. J. Zhang, *J. Electroceram.* **2007**, *19*, 113.
[3] J. Rodel, W. Jo, K. T. P. Seifert, E. M. Anton, T. Granzow, D. Damjanovic, *J. Am. Ceram. Soc.* **2009**, *92*, 1153.
[4] G. O. Jones, P. A. Thomas, *Acta Crystallogr. Sect. B-Struct. Commun.* **2002**, *58*, 168.
[5] A. M. Glazer, *Acta Crystallogr. Sect. B-Struct. Commun. B* **1972**, *28*, 3384.
[6] S. Gorfman, P. A. Thomas, *J. Appl. Crystallogr.* **2010**, *43*, 1409.
[7] E. Aksel, J. S. Forrester, J. L. Jones, P. A. Thomas, K. Page, M. R. Suchomel, *Appl. Phys. Lett.* **2011**, *98*, 152901.
[8] V. Dorcet, G. Trolliard, *Acta Mater.* **2008**, *56*, 1752.
[9] V. Dorcet, G. Trolliard, P. Boullay, *Chem. Mat.* **2008**, *20*, 5061.
[10] G. Trolliard, V. Dorcet, *Chem. Mat.* **2008**, *20*, 5074.
[11] D. I. Woodward, J. Knudsen, I. M. Reaney, *Phys, Rev B* **2005**, **72**, 104110.
[12] R. E. Eitel, S. J. Zhang, T. R. Shrout, C. A. Randall, I. Levin, *J. Appl. Phys.* **2004**, *96*, 2828.
[13] K. Z. Baba-Kishi, T. R. Welberry, R. L. Withers, *J. Appl. Crystallogr.* **2008**, *41*, 930.
[14] T. R. Welberry, D. J. Goossens, R. L. Withers, K. Z. Baba-Kishi, *Metall. Mater. Trans. A-Phys. Metall. Mater. Sci.* **2010**, *41A*, 1110.
[15] Y. P. Guo, Y. Liu, R. L. Withers, F. Brink, H. Chen, *Chem. Mat.* **2011**, *23*, 219.
[16] R. Comes, M. Lambert, A. Guinier, *Solid State Commun.* **1968**, *6*, 715.
[17] I. Levin, V. Krayzman, J. C. Woicik, J. Karapetrova, T. Proffen, M. G. Tucker, I. M. Reaney, *Phys. Rev. B* **2009**, *79*.
[18] F. A. Kassan-Ogly, V. E. Naish, *Acta Crystallogr. Sect. B-Struct. Commun.* **1986**, *42*, 325.
[19] R. L. Withers, in *Advances in Imaging and Electron Physics*, Vol *152*, (Ed: P. W. Hawkes) Elsevier Academic Press Inc, San Diego, **2008**, pp. 303.
[20] M. Groting, S. Hayn, K. Albe, *J. Solid State Chem.* **2011**, *184*, 2041.
[21] R. De Ridder, G. Van Tendeloo, S. Amelinckx, *Acta Crystallogr. Sect. A* **1976**, *32*, 216.
[22] D. Zhang, P. Oleynikov, S. Hovmöller, X. Zou, *Z. Kristallogr.* **2010**, *225*, 94.
[23] V. A. Shuvaeva, D. Zekria, A. M. Glazer, Q. Jiang, S. M. Weber, P. Bhattacharya, P. A. Thomas, *Phys. Rev. B* **2005**, *71*.
[24] B. P. Burton, E. Cockayne, in *Fundamental Physics of Ferroelectrics 2001*, vol. 582 (Ed. H. Krakauer) American Institute of Physics, Melville **2001**, pp. 82.
[25] J. Kling, S. Hayn, L. A. Schmitt, M. Groeting, H-J. Kleebe, K. Albe, *J. Appl. Phys.* **2010**, *107*.
[26] Y. Yan, S. J. Pennycook, Z. Xu, D. Viehland, *Appl. Phys. Lett.* **1998**, *72*, 3145.
[27] J. Sapriel, *Phys. Rev. B.* **1975**, *12*, 5128.
[28] R. Beanland, *Acta Crystallogr. Sect.* **2011**, *A67*, 191.
[29] Y. M. Jin, Y. U. Wang, A. G. Khachaturyan, J. F. Li, D. Viehland, *J. Appl. Phys.* **2003**, *94*, 3629.
[30] C. A. Randall, M. G. Matsko, W. Cao, A. S. Bhalla, *Solid State Comm.* **1993**, *85*, 193.
[31] A. A. Belik, S. Y. Stefanovich, B. I. Lazoryak, E. Takayama-Muromachi, *Chem. Mat.* **2006**, *18*, 1964.